Local geoelectrical models of the Martian subsurface for shallow groundwater detection using sounding radars

E. Heggy, P Paillou, F Costard, N Mangold, G Ruffie, F Demontoux, Gilles Grandjean, J. M Malézieux

Local geoelectrical models of the Martian subsurface for shallow groundwater detection using sounding radars

E. Heggy,[1,2] P. Paillou,[1] F. Costard,[3] N. Mangold,[3] G. Ruffie,[4] F. Demontoux,[4] G. Grandjean,[5] and J. M. Malézieux[6]

Received 15 February 2002; revised 20 July 2002; accepted 28 August 2002; published 6 March 2003.

[1] Low-frequency sounding radars should be able to probe the Martian subsurface layers down to varying depths, depending on the geoelectrical properties of the sounded sites. We present in this work four frequency-dependent geoelectrical models of the Martian subsurface in the 1–20 MHz frequency band, based on laboratory electromagnetic characterization of Martian soil analogues. Those models correspond to local Martian sites that we considered to be of particular interest in the search for water using mainly the Ground-Penetrating Radar (GPR) instrument of the Netlander mission. Results and discussion are also valid for both sounding experiments MARSIS and SHARAD. The four models of the Martian subsurface are designed to represent terrains where recent fluvial-like features suggest the presence of near-subsurface ground ice and probably liquid water. We performed measurements on volcanic and sedimentary materials that may be present on these sites under the appropriate geophysical conditions that may exist in those terrains. We then simulated the backscattered radar echo arising from each site in the 2 MHz frequency band, using the Finite Difference Time Domain (FDTD) algorithm, in order to evaluate the instrument performances to probe the subsurface stratigraphy of each site. Our results confirm that the near-subsurface rich iron oxide mineralogy controls the instrument performances in terms of penetration depth and signal-to-noise ratio in the 2 MHz frequency band. We finally discuss the geophysical and geoelectrical sounding conditions that could lead to an ambiguous detection of shallow subsurface water on Mars for the Netlander GPR. *INDEX TERMS:* 3210 Mathematical Geophysics: Modeling; 1794 History of Geophysics: Instruments and techniques; 5144 Physical Properties of Rocks: Wave attenuation; 5109 Physical Properties of Rocks: Magnetic and electrical properties; *KEYWORDS:* Mars, hydrology, GPR, sounding, simulation, FDTD

Citation: Heggy, E., P. Paillou, F. Costard, N. Mangold, G. Ruffie, F. Demontoux, G. Grandjean, and J. M. Malézieux, Local geoelectrical models of the Martian subsurface for shallow groundwater detection using sounding radars, *J. Geophys. Res.*, *108*(E4), 8030, doi:10.1029/2002JE001871, 2003.

1. Introduction

[2] Models of the thermal structure of the Martian crust suggest that the thickness of frozen ground (the depth at which the local temperature rises above the ice fusion point) range from ~2.5–5.0 km at the equator to ~6–12 km at the poles [*Clifford*, 1993; *Clifford and Parker*, 2001]. Recently, high-resolution images from the Mars Orbital Camera (MOC) on board the Mars Global Surveyor (MGS) orbiter reveal the possible presence of water layers in the near subsurface of Mars, at a depth of few hundreds meters. Water could flow out from an underground ice rich saturated layer covered locally by volcanic altered materials [*Malin and Edgett*, 2000a].

[3] Efficient sounding methods are required in order to detect the water present in the Martian subsurface a hundred meters or a few kilometers deep. One of the best suited is based on sounding radars. Water, even if still present on Mars at shallow depth (less then 300 m), will be difficult to detect using drilling and seismographs. Radar sounding methods, either from orbit or from surface based systems, represent the adequate geophysical tool to inform us about subsurface water abundance and distribution, a parameter of primary importance to understand the history of the planet [*Ori and Ogliani*, 1996; *Berthelier et al.*, 2000; *Clifford et al.*, 2001].

[4] Three radar instruments are planned in the current decade to probe the Martian subsurface and detect the presence and distribution of subsurface water layers. In 2003, the Mars Advanced Radar for Subsurface and Iono-

[1]Observatoire Astronomique de Bordeaux, Floirac, France.
[2]Also at Astronomy Department, Cairo University, Giza, Egypt.
[3]Université Paris-Sud, Orsay, France.
[4]Laboratoire de Physique des Interactions Ondes-Matière-ENSCPB, Talence, France.
[5]Bureau de Recherches Géologiques et Minières, Orléans, France.
[6]Institut Environnement, Géo-Ingénierie, Imagerie et Développement, Talence, France.

0148-0227/03/2002JE001871

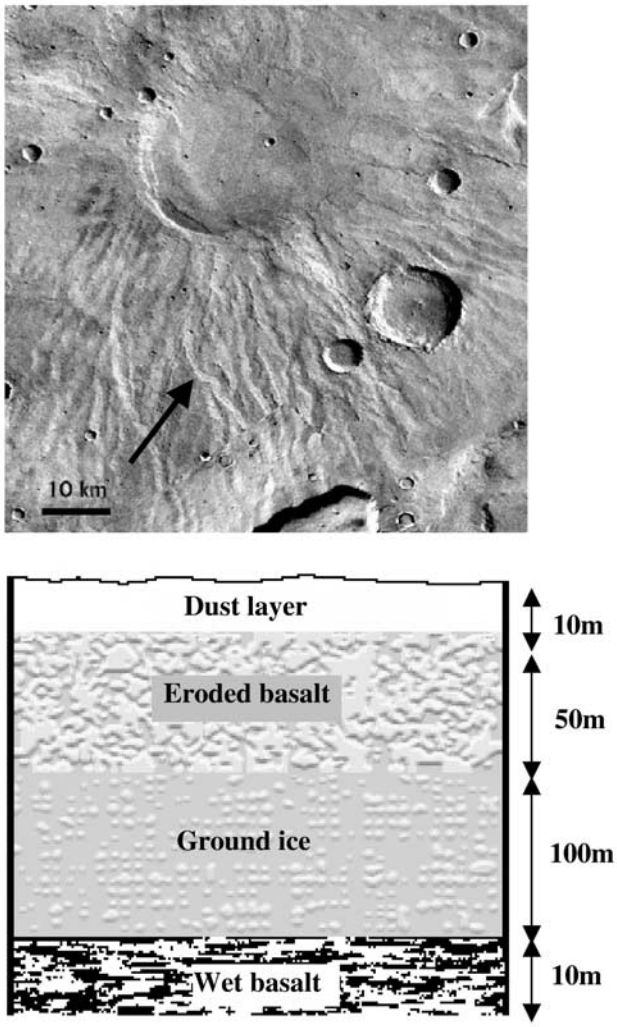

Figure 1. Top: the Viking image of the Hadriarca Pateraa volcano (31 S, 267 W). The arrow on the image shows Amazonian fluvial features formed by interactions of lava with water. Bottom: the proposed geological profile for a shallow aquifer associated with local geothermalism that might exist for similar sites.

sphere Sounding (MARSIS) experiment onboard the Mars Express ESA orbiter will be the first instrument to perform a global vertical sounding at the 2 MHz frequency [*Picardi et al.*, 1999]. It will be followed by the Ground-Penetrating Radar experiment; the Netlander mission in 2007, which will land four autonomous geophysical stations at different sites [*Berthelier et al.*, 2000]. These two experiments will mainly focus on the deep water detection, while a third instrument focused on Shallow Radar sounding (SHARAD) is planned for 2005 onboard the NASA Mars Reconnaissance Orbiter (MRO) will operate at a higher frequency around 20 MHz, in order to detect probable water Layers at shallow depth [*Beaty et al.*, 2001].

[5] The performances of all of these radar systems are strongly dependent on the petrology and mineralogy of the Martian subsurface [*Olhoeft*, 1998; *Heggy et al.*, 2001], which define the electrical behavior of each geological layer of the sounded sites. Most of the Martian surface presents a volcanic context and is covered by an iron oxide-rich dust layer, more probably constituted of altered basalts [*Pinet and Chevrel*, 1990], hematite [*Christensen et al.*, 2000], maghemite and other ferromagnetic minerals [*Hargraves et al.*, 1977]. This dust material is overlaying volcanic layers of fractured basalt and lava flows, with a geographically and stratigraphically variable component of massive and interstitial ice [*Clifford*, 1993; *Clifford and Parker*, 2001]. Deeper subsurface material could be mainly constituted of fractured ground ice [*Clifford and Johansen*, 1982]. If we assume this configuration to be representative of the Martian subsurface, then materials present in the first few hundred of meters of the subsurface could significantly attenuate the probing radar signal, due to electric and magnetic losses, thus limiting the penetration depth to few hundreds of meters at the 2 MHz frequency [*Heggy et al.*, 2001].

[6] Radar sounders should then operate at specific sites where the geoelectrical context is locally less conductive and where local geothermal conditions could lead to the presence of liquid water at shallow depths [*Clifford and Parker*, 2001]. In this paper, we present the geoelectrical modeling of such favorable sites in order to define future potential landing sites for the GPR experiment of the Netlander mission, and derive some criteria for optimal sounding sites for future radar experiments. Numerical simulations of the radar echo for the selected sites are presented and discussed.

2. Geological Models

[7] Four geological models of Martian subsurface are proposed in order to highlight the effect of several components such as liquid water, magnetic minerals and sedimentary deposits. The presence of fine grained or coarse deposits of different petrology (especially with varying porosity and permeability) may substantially affect the ice content in the subsurface and the radar signatures. These models correspond to possible local stratigraphy on Mars but large uncertainties exist about the composition and nature of the subsurface material. Examples are given to illustrate each proposed model refers to locations on Mars where the subsurface could correspond to the model, but detailed thickness and composition of the layers are speculative. These models do not take into account the regional variability of the selected geological unit. The possibility of finding shallow aquifers in the Martian near-surface is low due to cold temperatures, and liquid water should not be present at less than 1 km according to realistic thermal gradients [*Clifford*, 1993]. Nevertheless, we detail three examples where local residuals of subsurface water could be found at shallow depth. These locations would correspond to regions of high geothermal flow (2.1), outflow channels (2.2), or ice-rich northern plains (2.3). The last case (2.4) does not consider liquid water but sediments formed by desiccation of an ancient lake.

2.1. Shallow Aquifers Associated With Local Geothermal Anomalies

[8] Large geothermal gradients may occur within or near areas of recent volcanic activity. For example, the Hadriarca Patera volcano (31°S, 267°W) shows Amazonian fluvial

features formed by interactions of lavas with water as shown in the upper part of Figure 1 [e.g., *Allen*, 1979]. Lavas are likely filled by interstitial ice at several hundred meters deep because ground ice may not have been completely desiccated at the latitude of this volcano. Liquid water still could exist in the subsurface of the volcano if the thermal gradient is unusually high like in similar regions on Earth and if the subsurface material is not too thermally conductive to be frozen deeply due to the low surface temperatures. Such conditions would imply a subsurface stratigraphy such as in the bottom part of Figure 1: (1) 10 meters of dust covering the surface, (2) 50 m of eroded basalt corresponding to the porous part of basalt eroded by surface processes, (3) 100 m of basalt filled by interstitial ground ice and (4) a layer of wet basalt above the melting point. In this model we do not include magnetic minerals like maghemite in the subsurface layers.

2.2. Outwash Plains

[9] This model can correspond to a typical situation where outflow channels converge into the northern plains. A few billion years ago, large bodies of water could have been formed at the ends of the large outflow channels (Chryse and Acidalia Planitiae, Utopia Planitia, East of Hellas Planitia). This unit occupies the lowest areas within the channels and may contain volatile materials. According to the study of rampart craters, the thickness of the volatile rich layer of sedimentary deposits is estimated to be less than 800 m [*Costard and Kargel*, 1995]. In the proposed model, different layers are interpreted to be fluvial sediments up to 500 m in thickness. These sediments (both aeolian and fluvial deposits) are considered as an uncemented ground with porosity from 40% to 50%. These estimations are based on the bulk porosities of Martian soil as analyzed by the Viking Landers [*Clark et al.*, 1976; *Gooding*, 1978], as well as from model of the megaregolith proposed by *Clifford* [1993]. These outwash plains occupy a latitudinal band between 20° North and 45° South, which corresponds to a ground ice thickness of several kilometers. According to theoretical models [*Squyres et al.*, 1992; *Clifford*, 1993] as well as morphological analysis [*Costard*, 1989; *Kuzmin et al.*, 1988], a first zone extending down to 300 m is supposed to be desiccated (sublimation process). It corresponds to fluvial and volcanic episodes, as shown in Figure 2. The second zone, starting at 300 m, is assumed to be basaltic and filled with ground-ice down to 2500 m where the melting point is reached and liquid water is present. This region of fractured basaltic rock may persist to depths of 10 km or more [*Clifford*, 1993; *Clifford and Parker*, 2001]. Several investigators have emphasized magmatic activity in these areas in relationship with the Tharsis activity [*Tanaka and Chapman*, 1990]. It may have been responsible for the generations of liquid water by melting ground ice trapped in the underlying megaregolith [*Zimbelman et al.*, 1992].

2.3. Ejecta Deposits

[10] This model shown in Figure 3, corresponds to different geological units overlaid by ejecta deposits from impact craters. The uppermost part of the stratigraphy is a dry material made of aeolian deposits (dust layer). A second zone results from impact processes with a 50 m thick ejecta deposit. This value takes into account the thickness (from 40

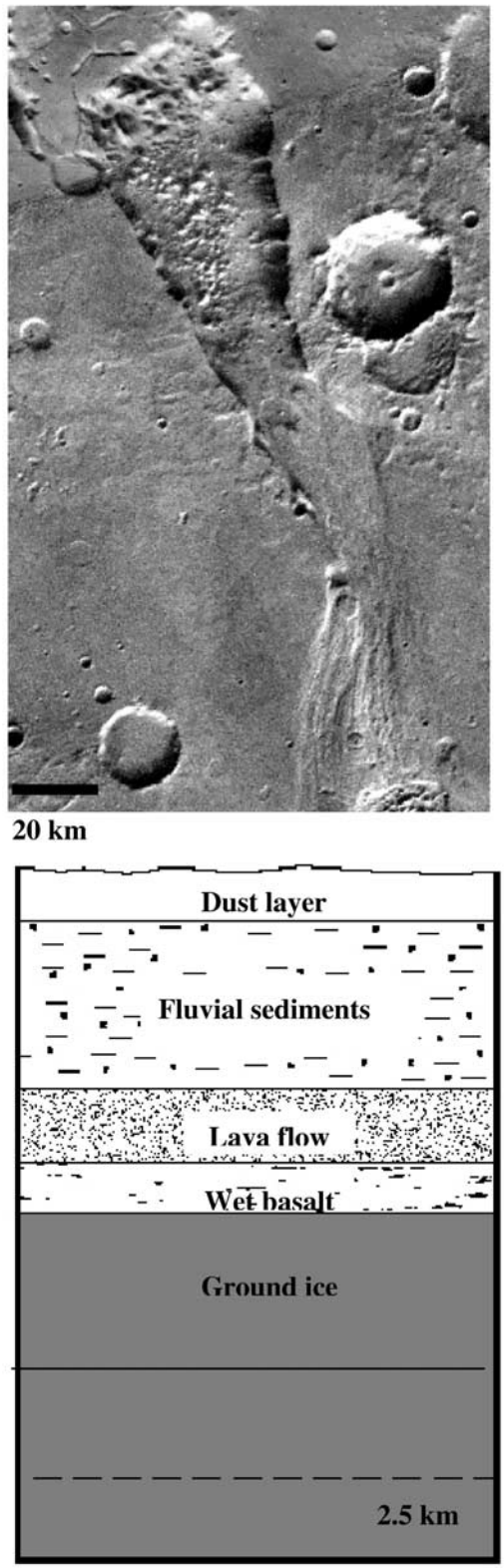

Figure 2. Top: the Outflow channel emerging from chaotic terrain (1 S, 43 W) (Viking image P-16983). Bottom: proposed geological model for this type of terrain where the presence of outflow channels may be interpreted by a rapid release of water from buried aquifers or the melting of ground ice by volcanism.

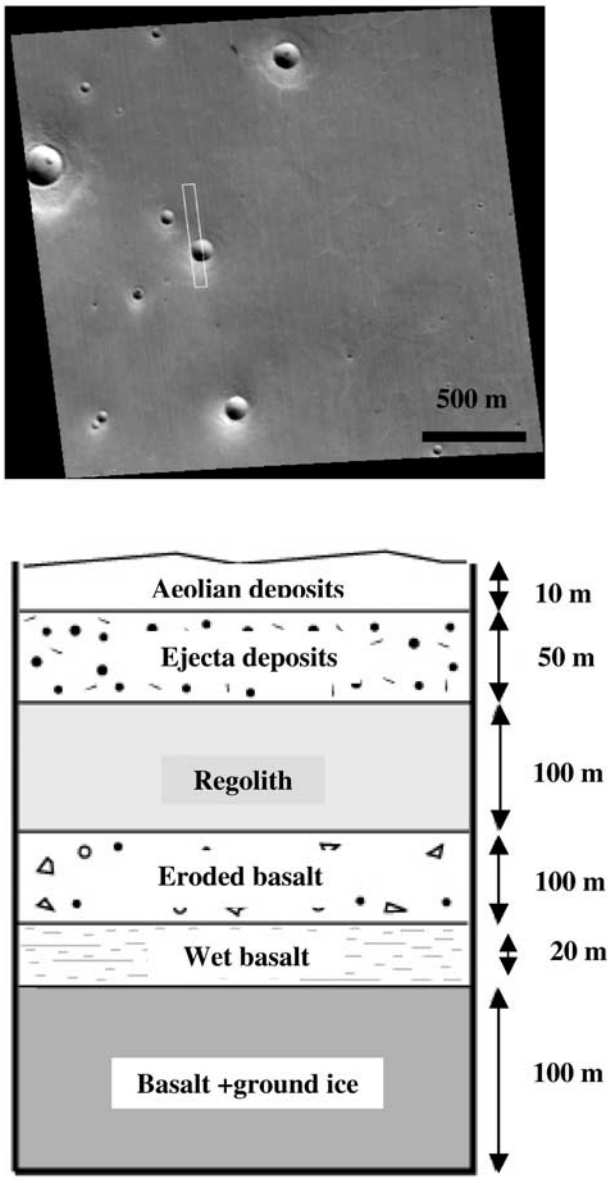

Figure 3. Top: the traverse across crater (30.3 N, 251.3 W) (MOC image M12-00506). Bottom: the corresponding geological model.

to 80 m) derived from MOLA profiles along some ejecta deposits [*Barlow et al.*, 2000]. The materials are interpreted to be impact-brecciated rocks at least for the upper layers. The porosity can be high and include a mixing of large amounts of substrate material into the ejecta deposit [*Melosh*, 1989] In the proposed model; these ejecta deposits overlay different layers of sediments and basaltic materials. These sedimentary deposits and, in particular locations, volcanic flows or deeper layers, may already contain ice. The lower limit of these layers is believed to be in the range of a few hundred of meters to 1 or 2 kilometers. As indicated above this is supposed to be an average situation, but current conditions may be very different from site to site.

2.4. Layered Deposits

[11] Layered deposits have been found in many regions with the Mars Global Surveyor camera [*Malin and Edgett*, 2000b]. The composition of layers is still unknown and a lot of speculations propose different compositions depending on whether the deposits have an aeolian, volcanic, fluvial or lacustrine origin. Interesting is a model containing evaporites that could correspond to layers formed by the drying of a stagnant lake like Sebkhas in terrestrial desert. Such conditions could correspond to the layers observed in closed depressions of Valles Marineris such as Melas Chasma (9°S, 77.5°W) (cf. MOC image M08-04367 in the top of Figure 4), or to layers inside craters like Gale or Henry. The layering proposed for such kind of geological setting is described in the bottom of Figure 4. The layer of mudstone is under erosion at the present time and could correspond to the eroded layers as shown by the arrow in the corresponding MOC image in the upper part of Figure 4. It is chosen to be mainly composed of kaolinite. This mudstone layer of 30 m thickness is underlain in the model by 30 m of gypsum ($CaSO_4$, 2H2O) and 30 m of aragonite ($CaCO_3$) lying over a basaltic basement. The chosen composition and thickness of the layers is one configuration among many different possible, but could likely correspond to Sebkha like deposits.

3. Electromagnetic Characterization and Geoelectrical Modeling

[12] Once the geological models are set and well defined, we investigated representative laboratory samples, in terms of mineralogy and porosity, for each layer of the above-discussed models. In our analogy, the electromagnetic properties of each layer of a geological profile are reduced to the electromagnetic characterization of the representative laboratory sample. Samples are compositionally homogeneous, with different porosities, temperatures and a varying amounts of iron oxide-rich minerals (hematite, maghemite, magnetite) for samples representing volcanic layers. It must be kept in mind that this is a simple approach that does not reproduce the heterogeneous composition of rocks and their complex porosity. However, as we are mainly interested in the permittivity of the samples to build geoelectrical models to evaluate losses in wave propagation, homogenous mixtures of minerals and ice are relevant. For the permittivity measurements, we used two capacitive cells. The first one characterizes powder materials (porosity ranging from 30 to 50%) and the second one measure pellets of compacted powder (porosity ranging from 15 to 30%) or machined from a rock sample. For the permeability measurements, we used a self-magnetic cell. More details concerning the measurement procedure and samples preparation have been described in earlier paper [*Heggy et al.*, 2001]. Each layer analog is described in terms of the real and imaginary part of its dielectric constant ($\varepsilon = \varepsilon' - i\varepsilon''$), its conductivity σ in S/m and its relative magnetic permeability μ (in this work we only considered the real part of the magnetic permeability, as mineral mixtures used to simulate the subsurface layers in the four models are not highly magnetic). It is important to note that the choice of analog materials to construct our samples is a first order approximation to illustrate the variation in the sounding radar performances in various possible Martian geoelectrical configurations.

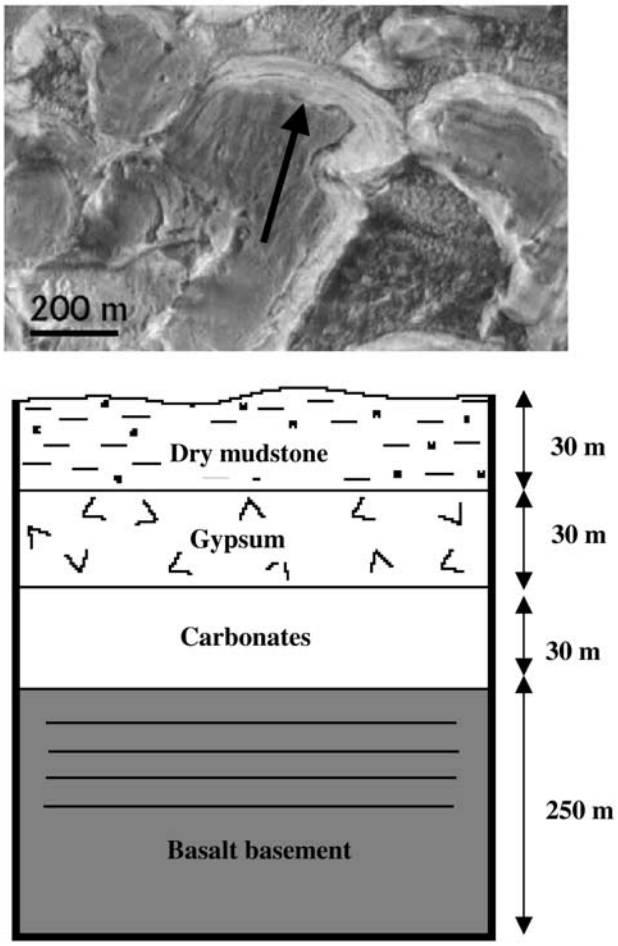

Figure 4. Top: MOC image of the Melas Chasma region (9 S, 77.5 W) (MOC image M08-04367). The arrow indicates what could represent a dry mudstone eroded layer. Bottom: the suggested model for this type of layered terrain.

[13] Tables 1, 2, 3, and 4 present the geoelectrical profiles for the geological models shown in Figures 1, 2, 3, and 4, respectively. In those models we assumed that the layers are homogenous and parallel according to the observed stratigraphy on the exposed wall rock of Valles Marineris [*McEwen et al.*, 1999]. The interfaces between layers have a step periodic roughness function with maximum amplitude of 1 m, which means that the shallow interfaces are relatively smooth compared to the wavelength inside the materials for 2 MHz radars. We introduced also a fuzzy level at each interface to take into account a short material transition gradient between each layer and possible unfrozen water concentration gradient [*Anderson and Morgenstern*, 1973].

[14] According to the surface chemical analysis of the Viking Landers and the Pathfinder mission suggest that the dust layer that covers the Martian surface can be assumed to be chemically homogenous [*Reider et al.*, 1997] for the major part of the planet. Thus we considered for the three models of Hadriarca Patera, ejecta deposits and outwash plains, the presence of a thin layer of dust (10 m). To simulate this dust layer, we mixed a dry basalt powder with a mass percentage of 7% of hematite, 7% of maghemite [*Hargraves et al.*, 1977] and 2% of magnetite, thus using a mean value of 15% of iron oxide concentration in the Martian surface dust layer. Its relative low dielectric value is due the high porosity around 50% (even if it is rich in iron oxides). Samples representing the dust layer have a grain size of 50 μm, which is the observed value for hematite grain size at the Martian surface [*Bell and Morris*, 1998]. For the samples representing the subsurface material, we considered a larger grain size (200 to 400 μm). This parameter is very important specially in measuring the sample magnetic permeability for iron oxide-rich materials, and it also controls the samples porosity. Another common layer for the three volcanic models is the water-saturated layer denoted by "wet basalt" in Figures 1, 2, and 3, which was simulated using water saturated basalt powder.

[15] The geoelectrical properties of the Hadriarca Patera volcano site are presented in Table 1. We simulated the second layer (eroded basalt) using a rock-machined pellet of Djiboutian basalt, which presents very similar chemical and physical properties to the rock analysis provided by the Viking and Pathfinder landers [*Paillou et al.*, 2001]. To simulate experimentally the third layer constituting the ground ice, we mixed a basalt powder to water and we compacted it to reach the lithospheric pressure at the corresponding depth in the geological model. The mixture was then put in a cold room down to the 210°K temperature. Special precautions were taken to ensure that samples (volcanic and ice mixed minerals) were free of moisture.

[16] For the outwash plains geoelectrical model presented in Table 2, we simulated experimentally the fluvial sedimentary layer, by measuring the permittivity of a powder of basalt mixed with 25% mass percentage of aragonite and dolomite at a porosity of 40%. For the lava and the ground ice layers, we used respectively a compacted dry basalt powder with a porosity of 35% and a basalt rock machined pellets with a lower porosity of 25% with ice inside the pores. We can clearly note the difference in their dielectric constant, which is mainly due to the difference in porosity between the two samples (which corresponds to a different lithospheric pressure in the geological profile). At a greater depth, we have a higher compaction leading to a lower porosity and thus a higher dielectric constant of the material.

[17] In the ejecta deposits model shown in Table 3, we used a low compacted basalt powder of 300 μm grain size mixed to the powder constituting the dust layer with 10% of ice. We mixed basalt and silicate to simulate the regolith layer. For the eroded basalt layer, we measured the permittivity of basalt mixed with 5% of hematite. As representative sample of the bottom layer in this geological profile, we used highly compacted basalt (porosity <20%). The dust layer and the wet saturated layer have been treated similarly as in the previous models.

[18] The layered deposits model presented in Table 4 corresponds to a quite different geological context. In this model, we did not introduce any ferromagnetic materials, (except at the bottom basalt bedrock) and we mainly used dry powder of kaolinite mixed to miner amount of materials described in the dust layer to estimate the permittivity of the first layer. The second layer was characterized with a gypsum compacted pellet, and we used an aragonite compacted pellet to simulate the possible presence of a carbonate layer in the Martian subsurface [*Fonti et al.*, 2001].

Table 1. Geoelectrical Model for a Shallow Aquifer Associated With Local Geothermalism[a]

	ε'		ε''		$\sigma\ 10^{-6}$, S/m		μ	
	2 MHz	20 MHz	2 MHz	20 MHz	2 MHz	20 MHz	2 MHz	20 MHz
Dust layer	3	2.7	0.25	0.22	28	240	1.5	1.1
Eroded basalt	8	7.2	0.5	0.45	56	500	1	1
Ground ice	7	6.3	0.1	0.0 7	5	12	1	1
Wet basalt	36	32	12	10.5	1344	11724	1	1

[a]Similar material can have different dielectric properties as the geophysical conditions (porosity, temperature, grain size) in each layer are different.

Finally for the basalt basement we used a compacted Djiboutian basalt powder.

4. Radar Echo Simulation

[19] The final step in our approach, to monitor the variations in the ability of the 2 MHz sounding radar instruments to detect the possible presence of shallow subsurface water in the Martian upper crust, is to simulate backscattered radar temporal response for each of the described sites. We used the Finite Difference Time Domain (FDTD) technique to solve the Maxwell equations and to obtain the magnitude of the backscattered electric field at each point inside the geoelectrical profile. Few electromagnetic methods can be adapted to describe properly the wave propagation in such relatively conductive materials. The advantage of the FDTD algorithm is its generality in terms of material, geometry and frequency [*Kunz and Luebbers*, 1993]. The method is a transient marching in time approach, in which time is divided into small discrete steps [*Yee*, 1966], and the geoelectrical model is built with elementary cubic cells in the simulation space. Each cell describes the relative permittivity, conductivity and relative permeability of the occupied volume. Once excited by the radar pulse, it gives the three-dimensional components of the electric and magnetic fields at each time step corresponding to the wave propagation across the geoelectrical model. We set the elementary cell dimension to be 5 m, in order to get the typical value of 10 cells per wavelength in the most conductive material in the profile (excluding the wet basalt layer), to obtain sufficient temporal accuracy and respect the algorithm stability conditions. To reduce the simulation noise, we used the Perfect Matching Layers (PML) algorithm as an electromagnetic absorbent around the simulation space.

[20] We simulated for each geoelectrical model presented in Tables 1 to 4 the case of 30 m mono-static monopole antenna in a perfect contact with the surface layer, which roughly corresponds to an ideal configuration of the Netlander GPR instrument. The emitted pulse is a spherical wave with maximum amplitude of 10 V/m. The emitted waveform is a modulated Gaussian vertically polarized, with a central frequency of 2 MHz and 2 MHz bandwidth. The same antenna measures the backscattered electric field echo **E** in the two cross polarizations Ex and Ey.

[21] We mainly considered the backscattered electric field in the X-directed polarization at the surface for each geoelectrical model. We used the Y-directed component of the backscattered field as an additional information source to distinguish between interface signal and simulation noise for low dynamic ranges (−150 to −200 dB). Simulations were performed in the time domain to observe reflections at each interface and thus evaluate the radar ability to penetrate down to the water-saturated layer for each of the volcanic model.

[22] Figure 5 shows the backscattered radar echo simulated for the four previously described geoelectrical models, at a 2 MHz frequency corresponding to the Netlander GPR characteristics. The results for each site are presented in two graphs. The upper graph indicates the losses in decibel versus the wave round trip time across the geoelectrical model. This informs us about the penetration depth corresponding to a given dynamic range. The lower graph shows the X component of the received electric field versus time, which illustrates the wave reflection at each geological interface. The dotted lines indicate the location of each subsurface interface calculated from the mean wave velocity inside each layer.

[23] The top left of Figure 5 (denoted by 2.1) presents the simulation of the geoelectrical model of a shallow aquifer associated with local geothermalism shown in Table 1 and Figure 1. We can see that the first three thin layers act as a single thick layer that absorbs exponentially the radar signal. The thickness of the first layers not being important compared to the wavelength inside the material, none of the interfaces could been identified on the backscattered echo. Even in the presence of a sufficient dielectric contrast, it is quite difficult to distinguish the second layer from the surface response at this frequency. The eroded basalt and the ground ice interface can be hardily distinguished by the mean of the backscattered electric field because of the low dielectric contrast at this interface. We can only note in this

Table 2. Geoelectrical Model for Outwash Plains in the Northern Hemisphere[a]

	ε'		ε''		$\sigma\ 10^{-6}$, S/m		μ	
	2 MHz	20 MHz	2 MHz	20 MHz	2 MHz	20 MHz	2 MHz	20 MHz
Dust layer	3	2.7	0.25	0.22	28	240	1.5	1.1
Fluvial sediments	5	4.4	0.5	0.46	56	513	1	1
Lava flow	7	6.2	0.5	0.3	56	335	1.5	1.3
Wet basalt	36	32	12	10.5	1344	11724	1	1
Ground ice	9	8	1	0.6	112	670	1	1

[a]Similar material can have different dielectric properties as the geophysical conditions (porosity, temperature, grain size) in each layer are different.

Table 3. Geoelectrical Model for the Fluidized Crater Ejecta Deposits[a]

	ε'		ε''		σ 10^{-6}, S/m		μ	
	2 MHz	20 MHz	2 MHz	20 MHz	2 MHz	20 MHz	2 MHz	20 MHz
Dust layer	3	2.7	0.25	0.22	28	240	1.5	1.1
Ejecta deposit	4	3.7	0.5	0.45	14	500	1	1
Regolith	14	12	0.7	0.6	77	670	1.2	1
Eroded basalt	9	8.1	0.2	0.2	22	220	1	1
Wet basalt	36	32	12	10.5	1344	11724	1	1
Basalt + ground ice	11	10	1	0.7	224	780	1	1

[a]Similar material can have different dielectric properties as the geophysical conditions (porosity, temperature, grain size) in each layer are different.

case the important reflection that occurs between the ground ice and the water-saturated layer, due to the strong dielectric contrast between the two materials. This is also visible in the corresponding reflection of the electric field plot, and corresponds to an attenuation of −50 dB that is in the detection range of the Netlander GPR and the MARSIS instrument too.

[24] For the outwash plains shown in the right upper part of Figure 5 (denoted by 2.2), we have a different situation where the interface between the dry sediments and the compact lava can be identified on the attenuation and electric field graphs, while even in the presence of a high dielectric contrast, it is difficult to distinguish between the compact lava layer and the water saturated basalt, because of the low dynamic at this depth (Figure 5, top right). An attenuation of −90 dB is still in the range of the Netlander GPR, but is behind the detectability limit for the MARSIS orbital experiment. After the water saturated layer, we can observe the decay in the radar signal as the wave travels in the ground ice and reaches a low dynamic point which is below the instrument limit.

[25] Results for the ejecta deposits site are presented in the bottom left part of Figure 5 (denoted by 2.3). The peaks on the attenuation (in dB) curve identify each geological interface. The thin water saturated layer does not show a strong signal as in the shallow aquifer case (Figure 5, top left), although being around the −60 dB level. This is due to a larger number of upper geological layers, causing strong multiple reflections, and then leaving less energy available at level of the water saturated layer. An important fact to be noted from these three previous simulations is the presence of the broadened region in the attenuation curves, which characterize the presence of water.

[26] The last case presented in the bottom right part of Figure 5 (denoted by 2.4) corresponds to the layered deposits terrain. This case presents geoelectrical properties very favorable for radar penetration, since materials constituting the first three layers contain no iron oxides. We have then there low dielectric losses and no magnetic losses. The first three layers are thin compared to the wavelength, and as they present no important dielectric contrast, we can hardly identify the location of each interface. Only the basalt basement can be distinguished. Such a geological model, even if it does not contain a water-saturated layer, suggests that low losses due to the low permittivity of the first subsurface layers could reflect the presence of carbonated material (in a geological context presenting adequate evidences of past hydrological sedimentary processes).

5. Discussion

[27] Numerical simulation of a 2 MHz electromagnetic wave propagating in the described geological models shows the variation in the radar ability to detect and distinguish the presence of a water saturated layer in terrains where we expect discontinuities in the ground ice thermal properties that might lead to the presence of liquid water in the first few hundred of meters of the Martian subsurface. We can mainly distinguish three cases:

[28] The first case corresponds to a volcanic context in which the radar pulse penetrates down to the water saturated layer, but due to the near subsurface stratigraphy, we cannot distinguish reflection on different geological interfaces and the one arising from the water-ground ice interface. This is the case of the radar echo simulation representing the ejecta deposits site. This is due to the presence of an important dielectric contrast between the other dry volcanic layers, which contains different amounts of iron oxides under different compaction levels (decreasing the porosity increases the dielectric constant and the conductivity).

[29] The second case is represented by the shallow aquifer associated with local geothermalism and the outwash plains. We observe here an exponential attenuation of the radar wave when propagating into the first subsurface layers, without any sharp reflection at the interfaces of the geological layers since they show low dielectric contrast. A stronger reflection can then be observed on the water-rich layer, producing a broadened region in the attenuation curves. It constitutes a kind of ideal case to detect and probably identify subsurface water, if the signal is not too attenuated by the first geological layers, as it is the case for outwash plains.

Table 4. Geoelectrical Model for the Layered Deposits Terrain[a]

	ε'		ε''		σ 10^{-6}, S/m		μ	
	2 MHz	20 MHz	2 MHz	20 MHz	2 MHz	20 MHz	2 MHz	20 MHz
Dry mudstone	3.2	2.8	0.2	0.1	24	120	1.2	∼1.1
Gypsum	4	3.8	0.6	0.5	67	560	1	1
Carbonates (aragonite)	6	5.7	0.1	0.1	12	110	1	1
Basalt basement	8	7.6	0.5	0.4	56	450	1	1

[a]Similar material can have different dielectric properties as the geophysical conditions (porosity, temperature, grain size) in each layer are different.

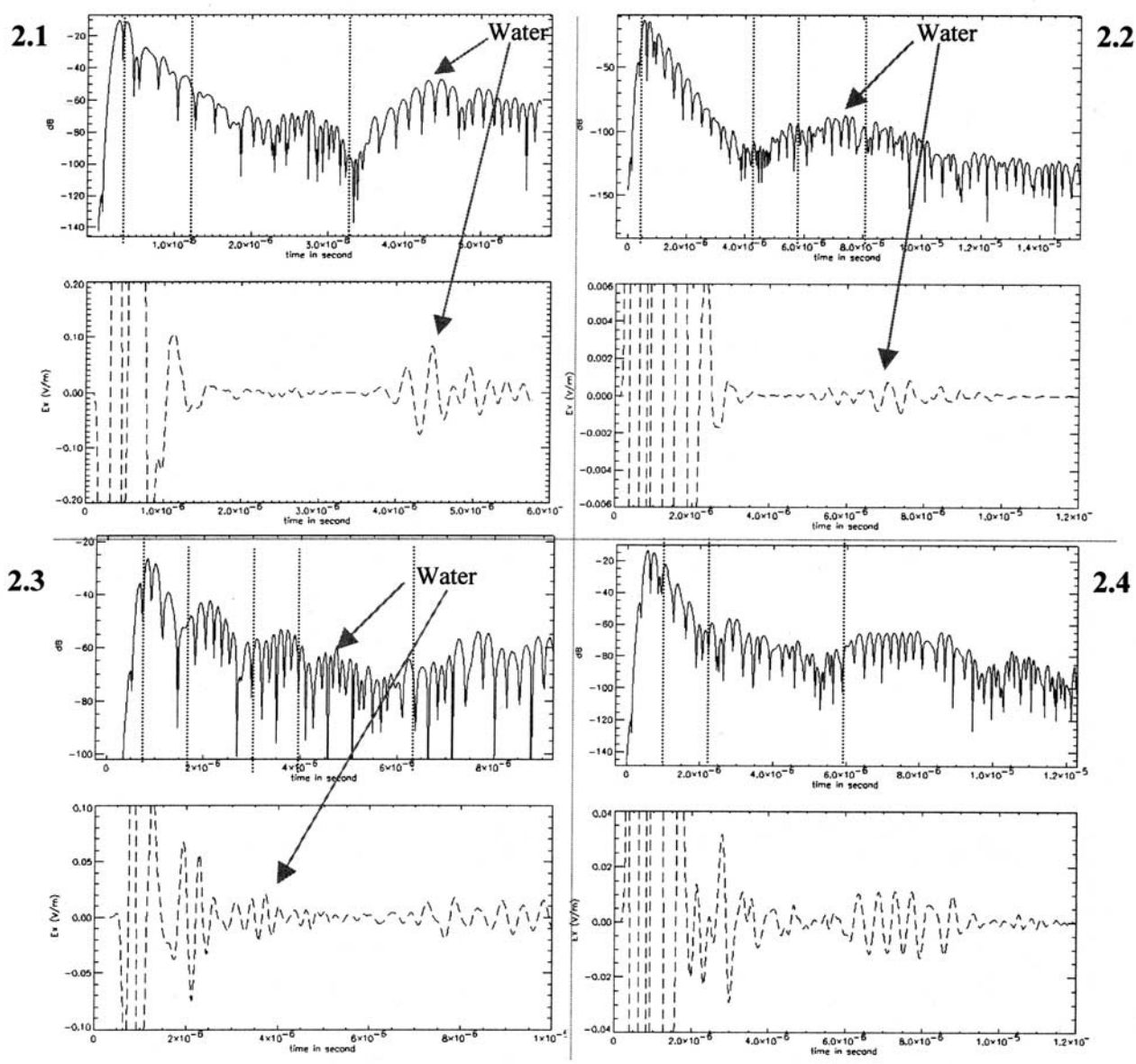

Figure 5. The 2 MHz radar echo simulations corresponding to the four geoelectrical models. Figures present the normalized losses in decibel (plain line) and the backscattered electric field versus the wave round trip time (dash line). The dotted lines indicate the location of each subsurface geological interface; high-resolution structures in the normalized loss curves represent the signal modulation and simulation noises. Top left: (2.1) shallow aquifer associated with local geothermalism. Top right: (2.2) outwash plains. Bottom left: (2.3) ejecta deposits model. Bottom right: (2.4) layered deposits terrain. The linear *Y* axis scale of the electric field plots has been reduced to visualize reflections from the third interface. Arrows indicate the signal peak corresponding to the water-saturated layer.

[30] The third case corresponds to a geoelectrical model free of water and iron-rich materials, such as the layered deposit terrains. Although the radar response from the basalt basement could be misinterpreted as a water-rich layer as the case of the outwash plains (compare the last peak in Figure 5, top and bottom right) a lower attenuation than the one observed in volcanic context (compare the attenuation slope in Figure 5, top and bottom right) could help detecting past hydrological sedimentary deposits (carbonates).

[31] In the simulation corresponding to the ejecta deposits model where the water-saturated layer is 260 m deep, the radar echo gives strong evidence of the presence of the subsurface-layered structure. Without a known first order geoelectrical model it is difficult to distinguish the signal corresponding to water interface. While in the case corresponding to the outwash plains the backscattered echo shows a clear response of the subsurface water interface at a deeper location (310 m), but with a strong attenuation of the first subsurface layers, leading to a poor signal-to-noise ratio. The most favorable case is represented by the Hadriarca Patera volcano site, for which volcanic materials presenting a reasonable attenuation factor cover a water-rich layer at a depth of 160 m. The radar signal associated with the wet basalt can be clearly observed, and remains in the

−60 dB attenuation range. Among the previous discussed models, terrains similar to the Hadriarca Patera site seem to be the most interesting sites for optimal subsurface water detection using sounding radar techniques, for both landed systems such as the GPR of the Netlander mission and orbital ones such as the MARSIS instrument. We then strongly recommend similar sites for radar shallow subsurface investigations.

[32] Further simulations at a 20 MHz frequency show similar capabilities for mapping the subsurface water presence in such favorable sites, but one should consider here possible additional losses due to volume scattering effect caused by rocks and fractures distribution in the superficial layers [*Beaty et al.*, 2001; *Heggy et al.*, 2002]. Criteria of radar detection of subsurface water in a similar context should not be limited to the depth at which it may be present. In particular, ejecta deposits terrains could be unfavorable cases for a 20 MHz orbital sounder, where the high dielectric constant of the first volcanic layers will decrease the wavelength to a critical value, that might then increase considerably the volume scattering effect, and perhaps totally screen a shallow ice-water interface. Similar phenomena have been observed in sounding temperate glaciers [*Watts and England*, 1976]. Thus we expect the performances of 20 MHz radar sounder to be more sensitive to the near subsurface petrology than for the 2 MHz case.

6. Conclusion and Perspectives

[33] We have investigated four models of the Martian subsurface that describe examples of sites presenting potential interest in the application of low frequency sounding radars to the search for water on Mars. We used laboratory measurements on sample analog and numerical FDTD simulations of the radar pulse propagation, to derive what might be an appropriate site to detect the possible presence of shallow water saturated layer using landed and orbital sounding radars. We suggest that regions such as the Hadriarca Patera volcano could present a potential type of terrain for future radar sounding of shallow aquifers. Sites representing possible subsurface hydrothermalism combined with a rather low attenuation factor of overlaying volcanic layers constitute a favorable site for sounding radar techniques. A reasonable penetration depth of hundreds meters at 2 MHz could allow the detection of liquid water at specific sites. Our simulations also showed that several geological interfaces in the Martian subsurface can present important dielectric contrasts due to different concentrations in iron-rich minerals and to variations in porosity and could give a similar radar response to the one expected from an ice-water interface at shallow depths. It is important to note that even using simple models, the radar echo simulation shows complex behaviors that could be interpreted since we know where geological interfaces are located. Working with future real data from the Netlander GPR instrument or similar sounder will imply a "blind" inversion process that will certainly be more complicated. It will in particular be very difficult to interpret the presence of any interface appearing on the radar echo without a preliminary study of the geological context for each site. We expect ambiguities to increase with increasing the depth of investigation.

[34] The reader must keep in mind that there is no unique description of the Martian geoelectrical properties, thus any sounding radar whether orbital or ground located cannot have a unique evaluation of performances, results will be strongly depending on the investigation site.

[35] The validity of the geological models presented and hence geoelectrical modeling and simulations is mainly related to our present-day knowledge of the Martian upper crust mineralogy and stratigraphy. We expect data from the Gamma Ray Spectrometer (GRS) and the Thermal Emission Imaging System (THEMIS) onboard the Mars Odyssey mission and future chemical and mineralogical analysis of the Martian soil to be performed by the 2003 Mars Exploration Rovers (MER) to provide the missing information concerning the chemical and mineralogical composition of the Martian surface. We should then be able to improve the modeling of a more realistic case of the Martian subsurface. Such work is crucial for preparing the interpretation of data that will be produced by the future radar instruments.

[36] **Acknowledgments.** The authors would like to thank J.P. Parneix for measurement and simulations facilities, J.J. Berthelier and the Netlander team for useful discussions.

References

Allen, C. C., Volcano-ice interactions on Mars, *J. Geophys. Res.*, *84*, 8048–8059, 1979.

Anderson, D. M., and N. R. Morgenstern, Physics, chemistry and mechanics of frozen ground: A review, North American contribution, paper presented at Ground Ice Second International Conference, Natl. Acad. of Sci., Reykjavik, 1973.

Barlow, N. G., J. M. Boyce, F. M. Costard, R. A. Craddock, J. B. Garvinb, S. E. H. Sakimato, R. O. Kuzmin, D. J. Roddy, and L. A. Soderblom, Standardizing the nomenclature of Martian impact crater ejecta morphologies, *J. Geophys. Res.*, *105*(E11), 26,733–26,738, 2000.

Beaty, W. D., S. M. Clifford, P. Gogineni, B. Grimm, C. Leuschen, G. Olhoeft, K. Raney, and A. Safaeinili, Analysis of the potential of a Mars orbital ground penetrating radar instrument in 2005, Mars Program Office White Paper, NASA Mars Program Off., Washington, D. C., 2001.

Bell, J. F., III, and R. V. Morris, Identification of hematite on Mars from HST, *Lunar Planet. Sci.*, *XXIX*, abstract 1751, 1998.

Berthelier, J. J., The GPR experiment on NetLander, *Planet. Space Sci.*, *48*, 1153–1159, 2000.

Christensen, P. R., M. Malin, D. Morris, J. Bandfield, M. Lane, and K. Edgett, The distribution of crystalline hematite on Mars from the thermal emission spectrometer: Evidence for liquid water, *Lunar Planet. Sci.*, *XXXI*, abstract 1627, 2000.

Clark, B. C., A. K. Baird, H. J. Rose, P. Toulmin, K. Keil, A. J. Castro, W. C. Kellihers, C. D. Rowe, and P. H. Evans, Inorganic analysis of Martian surface samples at the Viking landing sites, *Science*, *194*, 1283–1288, 1976.

Clifford, S. M., A model for the hydrologic and climatic behavior of water on Mars, *J. Geophys. Res.*, *98*, 10,973–11,016, 1993.

Clifford, S. M., and L. A. Johansen, Splash craters: Evidence for the replenishment of ground ice in the equatorial region of Mars, *Lunar Planet. Sci.*, *XIII*, 1982.

Clifford, S. M., and T. J. Parker, The evolution of the Martian hydrosphere: Implications for the fate of a primordial ocean and the current state of the Northern plains, *Icarus*, *154*(N1), 40–79, 2001.

Clifford, S. M., J. A. George, C. R. Stoker, G. Briggs, and D. W. Beaty, A proposal for an integrated geophysical strategy to "Follow the water" on Mars, paper presented at Conference on the Geophysical Detection of Subsurface Water on Mars, Lunar and Planet. Inst., Houston, Tex., 2001.

Costard, F., The spatial distribution of volatiles in the Martian hydrolithosphere, *Earth Moon Planets*, *45*, 265–290, 1989.

Costard, F., and J. Kargel, Outwash plains and thermokarst on Mars, *Icarus*, *114*, 93–112, 1995.

Fonti, S., A. Jurewicz, A. Blanco, M. I. Blecka, and V. Orofino, Presence and detection of carbonates on the Martian surface, *J. Geophys. Res.*, *106*(E11), 27,815–27,822, 2001.

Gooding, J. L., Chemical weathering on Mars: Thermodynamic stabilities of primary minerals (and their alteration products) from mafic igneous rocks, *Icarus*, *33*, 483–513, 1978.

Hargraves, R. B., D. W. Collinson, R. E. Arvidson, and C. R. Spitzer, The Viking magnetic properties experiments: Primary mission results, *J. Geophys. Res.*, *82*, 4547–4558, 1977.

Heggy, E., P. Paillou, G. Ruffié, J. M. Malézieux, F. Costard, and G. Grandjean, On water detection in the Martian subsurface using sounding radar, *Icarus*, *154*(N2), 244–257, 2001.

Heggy, E., P. Paillou, G. Ruffie, F. Demontoux, and G. Grandjean, Water detection in the Martian subsurface, paper presented at Ground Penetrating Radar Conference 2002, Univ. of Calif., Santa Barbara, 2002.

Kunz, K., and R. J. Luebbers, *The Finite Difference Time Domain Method for Electromagnetism*, CRC Press, Boca Raton, Fla., 1993.

Kuzmin, R. O., N. N. Bobina, E. V. Zabalueva, and V. P. Shashkina, Structure inhomogeneities of the Martian cryolithosphere, *Sol. Syst. Res.*, *XXII*, 195–212, 1988.

Malin, M. C., and K. S. Edgett, Evidence for recent groundwater seepage and surface runoff on Mars, *Science*, *288*, 2330–2335, 2000a.

Malin, M. C., and K. S. Edgett, Sedimentary rocks of early Mars, *Science*, *290*, 1927–1937, 2000b.

McEwen, A., et al., Stratigraphy of the upper crust of Mars, paper presented at 5th International Conference on Mars, Lunar and Planet. Inst., Pasadena, Calif., 1999.

Melosh, H. J., *Impact Cratering*, Oxford University Press, New York, 1989.

Olhoeft, G. R., Ground penetrating radar on Mars, paper presented at 7th International Conference on GPR, Univ. of Kansas, Lawrence, Kans., 1998.

Ori, G. G., and F. Ogliani, Potentiality of the ground-penetrating radar for the analysis of the stratigraphy and sedimentology of Mars, *Planet. Space Sci.*, *44*, 1303–1315, 1996.

Paillou, P., G. Grandjean, J.-M. Malézieux, G. Ruffié, E. Heggy, D. Piponnier, P. Dubois, and J. Achache, Performances of ground penetrating radars in arid volcanic regions: Consequences for Mars subsurface exploration, *Geophys. Res. Lett.*, *28*(5), 911–914, 2001.

Picardi, G., et al., The Mars advanced radar for subsurface and ionosphere sounding [MARSIS] in the MARS EXPRESS mission, paper presented at International Conference on Mars Exploration Program and Sample Return Missions, Cent. Natl. d'Etudes Spatiales, Paris, 1999.

Pinet, P., and S. Chevrel, Spectral identification of geological units on the surface of Mars related to the presence of silicates from Earth based near-infrared telescopic CCD imaging, *J. Geophys. Res.*, *95*, 14,435–14,446, 1990.

Reider, R. H., T. Economou, H. Wanke, A. Turkevich, J. Crisp, J. Bruckner, G. Dreibus, and H. Y. McSween Jr., The chemical composition of the Martian soil and rocks returned by the mobile alpha proton X-ray spectrometer: Preliminary results from the X-ray mode, *Science*, *278*, 1771–1774, 1997.

Squyres, S. W., S. M. Clifford, R. O. Kuzmin, J. R. Zimbelman, and F. Costard, Volatiles in the Martian regolith, in *Mars*, edited by H. H. Kieffer et al., pp. 523–554, Univ. of Ariz. Press, Tucson, 1992.

Tanaka, K. L., and M. G. Chapman, The relation of catastrophic flooding of Mangala Valles, Mars, to faulting of Memmania Fossae and Tharsis volcanism, *J. Geophys. Res.*, *95*, 14,315–14,323, 1990.

Watts, R. D., and A. W. England, Radio-echo sounding of temperate glaciers: Ice properties and sounder design criteria, *J. Glaciol.*, *17*, 39–49, 1976.

Yee, K. S., Numerical solution of initial boundary value problems involving Maxwell equations in isotropic media, *IEEE Trans. Antennas Propag.*, *14*(3), 302–307, 1966.

Zimbelman, J. R., R. A. Craddock, R. Greeley, and R. Kuzmin, Volatile history of Mangalla Valles, Mars, *J. Geophys. Res.*, *97*, 18,309–18,317, 1992.

F. Costard and N. Mangold, OrsayTerre, Bat. 509, Université de Paris-Sud, 91405 Orsay Cedex, France. (fcostard@geol.u-psud.fr; mangold@geol.u-psud.fr)

F. Demontoux and G. Ruffie, Laboratoire de Physique des Interactions Ondes-Matière-ENSCPB, 33402 Talence, France. (g.ruffie@piom.u-bordeaux.fr)

G. Grandjean, BRGM, BP 6009, 45060 Orleans, France. (g.grandjean@brgm.fr)

E. Heggy and P. Paillou, Observatoire Astronomique de Bordeaux, 2 rue de l'Observatoire, BP 89, 33270 Floirac, France. (heggy@observ.u-bordeaux.fr; paillou@observ.u-bordeaux.fr)

J. M. Malézieux, Institut Environnement, Géo-Ingénierie, Imagerie et Développement, Université de Bordeaux 3, 33400 Talence, France. (jmmalez@egid.u-bordeaux.fr)